Further Characterization of Rockwell Scientific LWIR HgCdTe Detector Arrays

Candice M. Bacon[a], Craig W. McMurtry[a], Judith L. Pipher[a], William J. Forrest[a], James D. Garnett[b], Donald Lee[b], and Dennis D. Edwall[b]

[a]University of Rochester, Rochester, NY, USA
[b]Rockwell Scientific Company, Camarillo, CA, USA

ABSTRACT

Future infrared space missions will undoubtedly employ passively cooled focal plane arrays (T $\sim$ 30K), as well as passively cooled telescopes. Most long-wave detector arrays (e.g. Si:As IBC) require cooling to temperatures of $\sim$ 6-8K.[1] We have been working with Rockwell Scientific Company to produce $\geq 10\mu$m cutoff HgCdTe detector arrays that, at temperatures of $\sim$ 30K, exhibit sufficiently low dark current and sufficiently high detective quantum efficiency, as well as high uniformity in these parameters, to be interesting for astronomy. Our goal is to achieve dark current below the target value of $\sim 30e^-/s$/pixel with at least 60mV of actual reverse bias across the diodes at T $\sim$ 30K. To this end, Rockwell Scientific Company has delivered three 10μm cutoff HgCdTe low dark current detector arrays with small capacitance diodes for characterization in Rochester. The most recent presentation[2] showed the remarkable preliminary performance of the first of these devices. We present further results on the first device along with results on the subsequent two deliveries.

Keywords: Long Wave InfraRed (LWIR) Detector, HgCdTe, Dark Current, Diode Characterization, Infrared Space Missions, Passive Cooling

1. INTRODUCTION

The infrared range from 5μm to 10μm is of interest for many proposed space astronomy missions (e.g. TPF and SIM). However, for this wavelength region, current technologies require onboard cooling mechanisms to operate infrared detector arrays, which can drive up the cost of space experiments. Future space telescopes with proper design will be able to attain focal plane temperatures down to $\sim$ 30K via passive cooling. Therefore, we are currently working with Rockwell Scientific Company to develop 10μm cutoff HgCdTe low dark current detector arrays optimized for operation at or above this temperature, that also exhibit adequate well depth to be useful for astronomy.

Large strides have been made in the realization of detector arrays that meet this objective. At the 2002 Hawaii SPIE meeting (Bacon et al. 2003),[3] we reported on a Long Wave Infrared (LWIR) 256×256 HgCdTe detector array with 9 different diode structures bonded to a NICMOS3 multiplexer and cooled to 30K. The best structures (small diodes) exhibited $\sim 30\%$ of pixels with dark currents $< 100e^-$/s. In 2003, preliminary measurements of the first of three large format detector arrays were reported at the San Diego SPIE meeting (Bacon et al. 2004)[2] two weeks after delivery. These detector arrays exploited the best diode structure determined previously, with high quality MBE[4] growth, and a 512×512 format detector array bonded to a HAWAII-1RG multiplexer. We reported that relatively low doping HgCdTe technology,[5] as well as advanced processing and bonding procedures, have led to exceedingly good dark currents well below the revised target dark current of $30e^-$/s over a large percentage of the array.

Here we delve further into characterization of the first device (H1RG-16-001, with a 9.1μm cutoff) and present results on the subsequent two deliveries, H1RG-16-002 and H1RG-16-003, with cutoffs of 8.4μm and 8.5μm respectively.

Further author information:
E-mail: candice@astro.pas.rochester.edu

2. DATA ACQUISITION AND REDUCTION

The HAWAII-1RG multiplexer is a 1024×1024 pixel read-out integrated circuit (ROIC), with four rows and columns of reference pixels around the perimeter. This leads to 1016×1016 active pixels. It has a selectable number of outputs, plus numerous other features. The HAWAII-1RG is identical in all features and functions to the HAWAII-2RG (see Loose et al. 2003)[6] except for the pixel format (1024×1024 vs. 2048×2048) and number of outputs (1, 2, 16 vs. 1, 4, 32). The HAWAII-1RG was operated in two-output "normal read-out mode"* with 100 kHz pixel read rate. We used a fast row-by-row reset followed by either partial or full array reads. Because we were concerned that this read-out mode might lead to variable amounts of debias because the reset to pedestal delay increased from the first to the last pixel read (i.e. for a full frame read this corresponds to an increase in reset to pedestal delay time from 1.5ms to 1.57s), we were careful to employ experimental methods which took this concern into account. These methods will be described in Section 3. Pixel by pixel reset and the HAWAII-1RG enhanced clocking mode† would have made dark current characterization at early integration times much easier, though we had not implemented that clocking scheme at the time the data were obtained.

While the HAWAII-1RG has an 18μm pixel pitch designed for SWIR and MWIR HgCdTe, we desire a 36μm pixel pitch for LWIR HgCdTe. Thus the LWIR HgCdTe detector array was bonded to every other pixel of the HAWAII-1RG, resulting in an effective array size of 512×512 (508×508 active) pixels. While these devices do not utilize microlenses despite a much smaller diode size than the pixel pitch (36μm), we plan to implement microlenses in future deliveries to optimize quantum efficiency and fill factor.

The majority of these data were taken in sample up the ramp (SUTR) mode in order to obtain many points on the integration ramp. This enables easier cosmic ray correction as well as, in some cases, noise characterization. In this mode, many frames (single reads of the device) are recorded. Other data were taken with Fowler sampling[7] to obtain multiply sampled images (multiple correlated frame reads) where a single Fowler sample pair (Fowler-1) is equivalent to correlated double sampling (CDS).

Data reduction was done primarily with Interactive Data Language (IDL). Several improvements over last year's reduction programs enabled more accurate characterization, especially with dark current. Biases as high as 200mV were applied, and all data were taken at approximately 30K.

3. DARK CURRENT AND WELL DEPTH

Prior results reported[3] did not employ the experimental methods discussed below, and included pixels with small well depths. Therefore the useful dark currents of these arrays are not as uniformly low as previously reported,[3] but are still extremely low for a large percentage of array pixels. Dark currents were obtained on a pixel by pixel basis as soon after the reset as practicable. In order to obtain this result, many partial array frames were combined into a full array frame in order to minimize the reset to pedestal delay times for each pixel. These frames will be referred to as *composite* frames. In addition to this, full array frames were also taken in sample up the ramp (SUTR) mode, and these will be referred to as *full* frames.

We found percentages of saturated, high dark current ($> 30e^-$/s), low dark current ($< 30e^-$/s), and ultra-low dark current ($< 1e^-$/s) pixels in our dark current characterization of these devices (see Tables 1 and 2).

Table 1. This table shows the percentage of pixels that are saturated in each of the three arrays at 0mV applied bias. These pixels are randomly distributed.

	H1RG-16-001	**H1RG-16-002**	**H1RG-16-003**
Saturated Pixels	8.5%	7.6%	7.2%

Though the low dark current pixels with sufficient well depth exhibited linear dark charge vs. time curves, even pixels with relatively low dark current can exhibit a non-linear dark charge vs. time curve. Two examples

* "Normal read-out mode" is a method of reading out the device, which is detailed in the HAWAII-1RG User's Manual. In short, it involves resetting the entire device row-by-row, then reading the pedestal and subsequent frames.

† This clocking mode enables integration times shorter than a frame time during a full frame read.

of pixels with these various dark currents are shown in Figure 1 along with a fit created by the method described below.

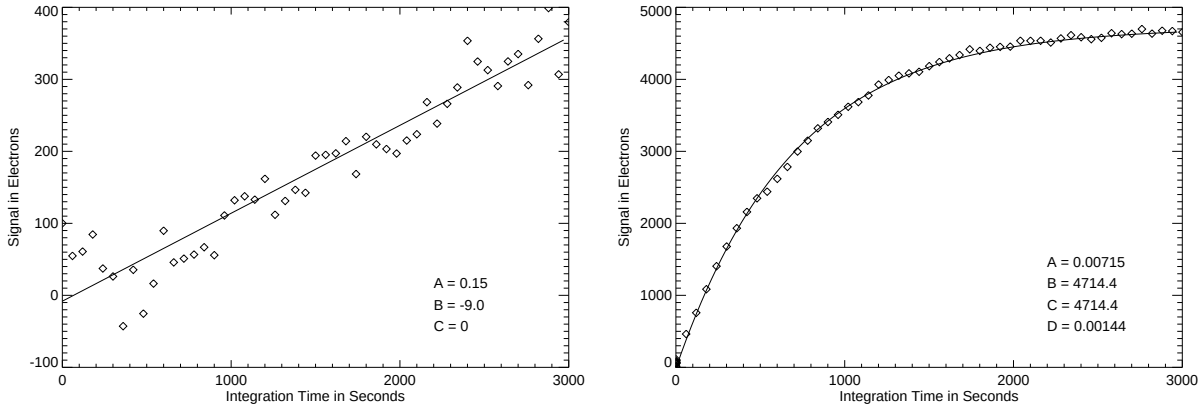

Figure 1. ***Left*****:** This graph shows the dark charge vs. time in SUTR mode for a single pixel from detector H1RG-16-001 exemplifying a linear dark charge vs. time curve (where $C = 0$ in Equation 1) in addition to ultra-low dark current ($\sim 0.15e^-$/s) at 0mV applied bias. This pixel has approximately 62mV ($\sim 41000e^-$) of well depth. All low and ultra-low dark current pixels exhibit linear dark charge vs. time curves. To see the percentages of pixels with low and ultra-low dark current, see Table 2. ***Right*****:** This graph shows the non-linear dark charge vs. time curve in SUTR mode for a single pixel from detector H1RG-16-001. This pixel has dark current as high as $\sim 7.0e^-$/s at 0mV applied bias. Though the pixel appears to be reaching saturation (see Section 5), we have evidence that suggests the saturation level is in fact much higher than $4700e^-$. The cause of this unusual behavior is under investigation.

In order to measure and accurately characterize the various ranges of dark current, two sets of data were taken: composite data (15 to 20 frames 100ms apart in SUTR mode) and full frame data (52 frames 60 seconds apart in SUTR mode). The first composite frame in the series is referred to as the composite pedestal, since it is the first frame read after the reset. We plot the dark charge, $F(t)$, vs. t, the actual time after the pedestal for each data point and subsequently fit with the empirical function in Equation 1, where A, B, C and D are fitting parameters. At any point in time on the dark charge vs. time fit, the dark current is given by the time derivative, $F'(t)$, of Equation 1. The function in Equation 1 was chosen to accurately characterize the linear and non-linear behaviors over the range of integration times observed.

$$F(t) = At + B - Ce^{(-Dt)} \tag{1}$$

For each pixel, the recorded dark current is $F'(0)$, the dark current at the time the pedestal was read. To complement the dark current measurement for each pixel, we measured the corresponding well depth (i.e. at t=0).

The well depth was determined by illuminating the detector array with a relatively low flux so that the degree of forward bias at saturation is at a minimum. We took full frame data in SUTR mode (110 frames 2 to 4 seconds apart), and ensured that the pixels were indeed saturated after 110 frames. We found the maximum value reached (in ADU) in that time for each pixel and created a saturation map, then determined actual well depth by subtracting the dark composite pedestal frame from the saturation map. The data were then linearized. There is a range of well depths after linearization, but a histogram of well depths peaks around the expected value, given by the addition of the applied bias to the pedestal injection of approximately 50mV (e.g. an applied bias of 50mV corresponds to an expected well depth of 100mV), for each applied bias.

In Table 2, we report percentages of pixels with at least the minimum well depth shown and dark current less than the maximum dark current shown at the given applied bias. The minimum well depth requirement in this table is 80% of the expected well depth. An example of the distribution of dark currents for pixels with

greater than 40mV of well depth at 0mV applied bias is shown in Figure 2. Pixels meeting these requirements are randomly distributed throughout the array.

Table 2. This table shows the performance of all three detectors under the constraints of dark current less than the goal of $30e^-/s$ and well depth greater than the expected well depth (given by the addition of the applied bias to the pedestal injection of approximately 50mV). Pixels that meet these requirements are randomly distributed.

Detector Performance

Applied Bias (mV)	**Well Depth Greater Than (mV)**	**Dark Current Less Than (e^-/s)**	**-001**	**-002**	**-003**
0	40	30	75.0%	76.2%	74.4%
		1	67.4%	69.9%	72.2%
50	80	30	50.9%	68.1%	69.4%
		1	27.9%	25.0%	55.7%
100	120	30	25.0%	53.8%	55.4%
		1	10.8%	5.92%	37.6%
200	200	30	2.07%	16.4%	24.3%
		1	0.30%	0.71%	10.6%

We obtained a statistical sample of well depth and dark current for arrays H1RG-16-002 and H1RG-16-003, by analyzing sub-array boxes, for two reasons. First, the arrays were not fully illuminated in our dewar. Second, there were defects on each of the two arrays that increased in size with increasing bias. Thus the boxes were chosen to exclude both the vignetted portions of the illumination and the defects at all applied biases for the dark current and well depth analysis. All boxes chosen for other analyses in this paper exclude the defects for the biases at which the data were taken.

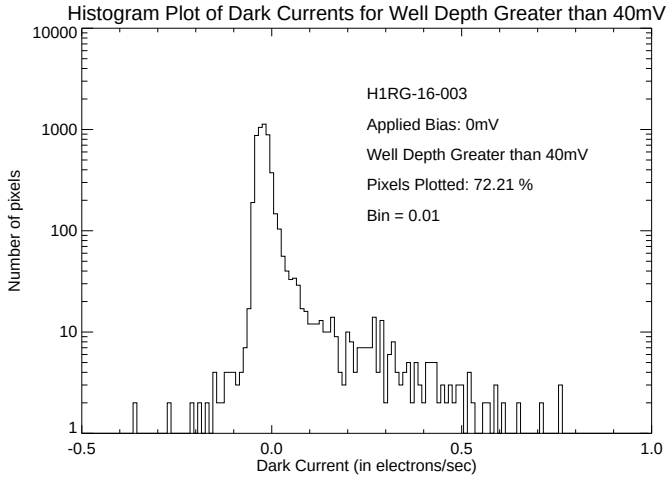

Figure 2. This graph shows the peak of the dark current histogram for detector H1RG-16-003.

In order to isolate pixels with similar dark current and well depth, the remainder of the data reduction was done only on the pixels that meet our dark current goal of $< 30e^-/s$ and fit the well depth requirement in Table 2. Thus, a pixel mask was created in software for each array to select only these pixels for the following analyses.

4. CAPACITANCE

Using the noise squared vs. signal method,[8] the capacitance and e^-/ADU were calculated.[‡] Forty Fowler-1 *images* (sample pairs) for each of 6 integration times were taken. These data were obtained by viewing an external blackbody source through a cold, narrow band 3.3μm filter for H1RG-16-001 and H1RG-16-002 and the K (2.23μm) filter for H1RG-16-003. The capacitance was determined on a box by box basis. An 8×6 grid of boxes were used, each of size 20×20 pixels in the central portion of each array. The capacitance was determined as follows from the masked pixels described within each of these boxes.

For each box and pair of *images* (20 pairs per integration time), the signal and noise were determined. To find the signal, we calculated the mean value of each pair of images individually for the accepted pixels within each box. For a corresponding spatial measurement of the noise, the standard deviation (divided by the square root of two) of the difference of the same pair of images and pixels was calculated. Then, the noise squared was plotted vs. signal for each box, with each pair of images yielding one point on the plot. The slope of the resulting line fit corresponds to the number of e^-/ADU for our system and hence capacitance.[8] The capacitances and e^-/ADU for all boxes were examined and the statistics are given in Table 3. For subsequent data reduction, the *median* values are used.

Table 3. This table shows capacitance measurements for all three detectors at 0mV applied bias. The median value for capacitance is used in all data reduction.

Capacitance and e^-/ADU

Detector	**H1RG-16-001**		**H1RG-16-002**		**H1RG-16-003**	
Statistic	*Capacitance (fF)*	*e^-/ADU*	*Capacitance (fF)*	*e^-/ADU*	*Capacitance (fF)*	*e^-/ADU*
Mean	97.8	4.07	106.8	4.44	105.8	4.4
Median	101.4	4.22	106.2	4.42	103.9	4.32
Std Dev	14.24	0.59	12.47	0.52	13.5	0.56

5. LINEARITY

Detector response under constant flux is non-linear with increasing exposure time, because the device debiases with increasing fluence. Given C is the nodal capacitance, the signal rate is proportional to $1/C$. The normalized signal rate is therefore given by C_0/C, where C_0 is the capacitance at zero signal. An effective means of measuring the non-linearity is by calculating the slope of the plot of normalized signal rate (C_0/C) vs. signal (Hora et al.).[9] Non-linearity was determined by using the same data that were used to measure well depth. The pixel mask described in Section 3 was used, and for these pixels normalized signal rate was plotted vs. signal.

The plots of C_0/C vs. signal exhibited a range of non-linearity for the pixels in each array. Some pixels showed extremely flat behavior while others had relatively steep negative slopes. Still, others had slight positive slopes for various possible reasons (such as a significant first frame effect[9]). Because of the range of non-linearity, the slope of a linear fit from 20% to 80% of saturation was plotted in a histogram for pixels used in the analysis, where the resultant distribution was Gaussian with a tail. The mean of the Gaussian, and the corresponding deviation from linearity at saturation is shown in Table 4. The non-linear behavior of a typical pixel from detector H1RG-16-001 can be seen in Figure 3.

[‡]The values reported[2] in 2003 were misleading since the analysis included pixels which did not meet the qualifications of Table 2.

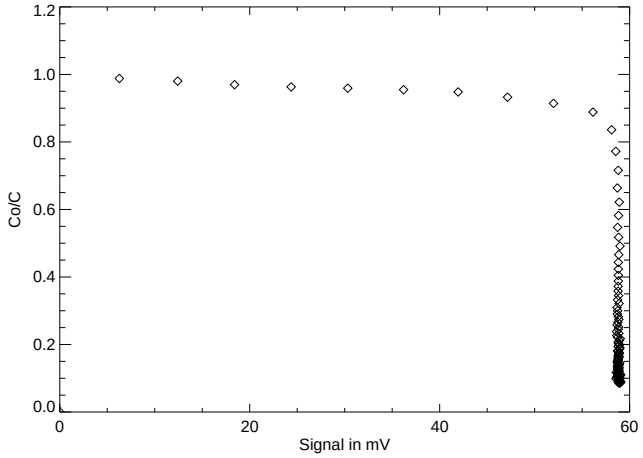

Figure 3. This is an example of the non-linear behavior of a typical pixel from detector H1RG-16-001.

Table 4. This table shows linearity measurements for all three detector arrays. The slopes of a fit to the linear region in C_0/C, for signals from 20% to 80% of saturation, were plotted in a histogram for pixels used in the analysis. The resultant slope distribution was Gaussian with a tail, and the mean of the Gaussian is given in the table along with the corresponding deviation from linearity at saturation. Data shown here were taken at 0mV applied bias.

Detector	**Mean Slope of C_0/C vs. Signal in $1/e^-$**	**Percent Non-Linearity at Saturation**
H1RG-16-001	-2.6×10^{-6}	8.2%
H1RG-16-002	-1.9×10^{-6}	7.2%
H1RG-16-003	-1.0×10^{-6}	4.4%

6. QUANTUM EFFICIENCY

Even though these devices are neither anti-reflection coated nor polished, the measured quantum efficiency (QE) was substantial (see Figures 4, 5 and 6). The QE can be no greater than 70 percent, due to reflection loss, and we expect that the small (as compared with pixel pitch) diode size is the dominant component of the lower measured QE per pixel. We fully expect to be able to compensate for these losses using microlenses and anti-reflection coatings.

The quantum efficiency for all three detectors was determined using a circular variable filter and a calibrated thermal illumination source. The data were taken with a Lyot stop of 50μm. There were 8 Fowler-1 *images* taken at each wavelength so that a detective quantum efficiency measurement could verify the responsive quantum efficiency measurement. As with the capacitance data, the pixel mask described in Section 3 was used. Signals from the mask-selected pixels within a user defined box[§] were averaged. The average signal obtained (S) was then compared to the expected signal in incoming photons (S_0) to determine responsive quantum efficiency,[10] as illustrated in Equation 2.

$$RQE = \frac{S}{S_0} \tag{2}$$

A spatial noise measurement, (N), was obtained from the standard deviation (divided by the square root of two) of masked pixels in the difference of two images. Since there were eight images, the median noise of the

[§]For these data, the box used was the same for all three arrays and centered in the illumination. The box had dimensions of 15×59. This not only avoided the vignetted regions, but since we were using a circular variable filter, it helped to ensure we were reporting values for the central wavelength.

four difference images was used. Likewise, the median signal of the four averaged images was used. The signal (determined as described above) to noise ratio compared to the expected signal in incoming photons yielded detective quantum efficiency,[10] as in Equation 3.

$$DQE = \frac{(\frac{S}{N})^2}{S_0} \tag{3}$$

The results are shown in Figures 4, 5, and 6. Though the large differences between responsive quantum efficiency

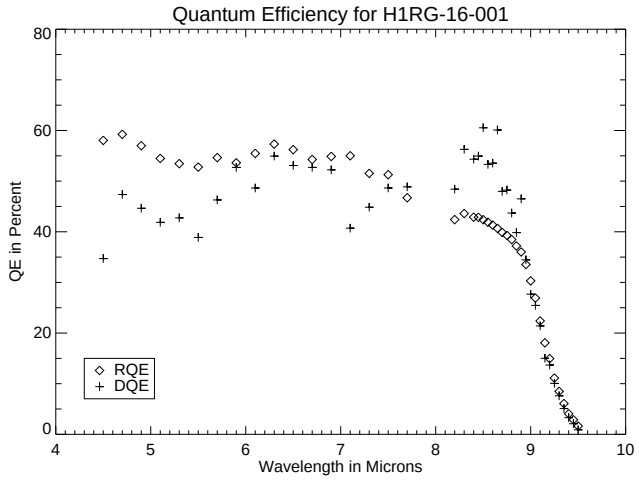

Figure 4. This graph shows both detective and responsive quantum efficiencies for selected pixels (as described above) of detector H1RG-16-001. Defining the cutoff wavelength to be the half power point of detector response, the cutoff wavelength is determined to be 9.1μm. The proximity of the signal to saturation between 8μm and 9μm caused errors in the noise determination (see Pain and Hancock[11] 2003), which in turn produced an incorrect DQE in this wavelength range.

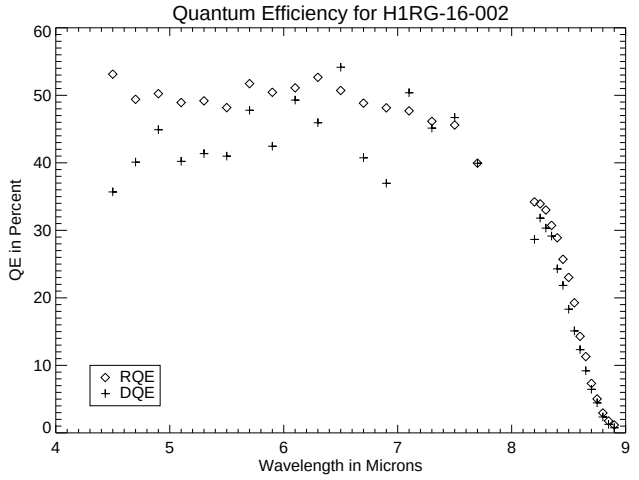

Figure 5. This graph shows both detective and responsive quantum efficiencies for selected pixels (as described above) of detector H1RG-16-002. Defining the cutoff wavelength to be the half power point of detector response, the cutoff wavelength is determined to be 8.5μm.

and detective quantum efficiency could imply gain at wavelengths below 5μm, because of scatter in the deduced QEs, this conclusion is premature. We intend to investigate this further with anti-reflection coated devices.

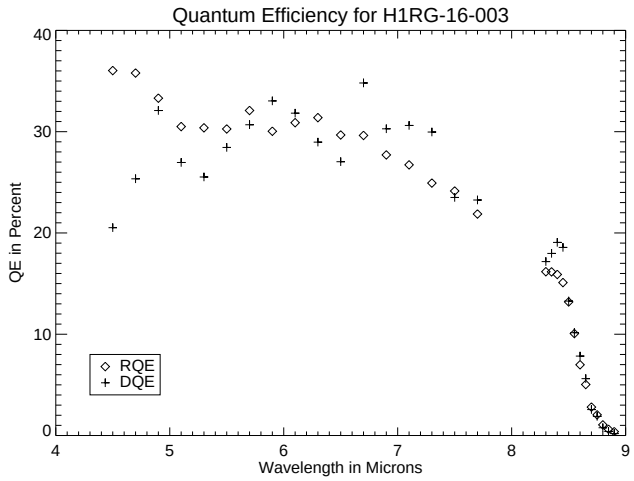

Figure 6. This graph shows both detective and responsive quantum efficiencies for selected pixels (as described above) of detector H1RG-16-003. Defining the cutoff wavelength to be the half power point of detector response, the cutoff wavelength is determined to be 8.4μm. The significantly lower QE on this device, as compared with the other two devices, may be related to noticeable irregularities on the surface of the device.

7. NOISE

We have not measured the noise for the majority of excellent pixels on these arrays because the noise was not the focus of this study. However, based upon graphs of dark charge vs. time (see Figures 1*(left)*, 7, and 8, which show an approximate peak to peak noise of 150e^-), a rough estimate of RMS noise (read noise per sample) for the well-behaved pixels in these devices is $\sim 30e^-$. This would lead to $\sim 42e^-$ of read noise for a Fowler-1 (CDS).

Even though this study did not focus on noise, during dark current characterization we discovered that a very small fraction of pixels exhibited an unusual noise characteristic. We then investigated the spurious noise to determine its origin, which we attribute to the multiplexer. From graphs of dark charge vs. time, we found that the dark charge made rapid transitions in both the positive and negative directions with respect to the overall dark current trend, which is a trademark of popcorn noise or burst noise.

Popcorn noise or burst noise is a term used to characterize rapid level shifts. Several types of popcorn noise have been exhibited by these arrays. One type has slow transitions which have a long time increment (approximately 400 seconds) between signal level shifts, as demonstrated in Figure 7.

Another has fast transitions which have very short time increments (less than 60 seconds) between signal level shifts, as demonstrated in Figure 8. Often the levels tend to jump by approximately the same amount every time, so that there appears to be a bifurcation into two levels. Sometimes there can be more than two levels, and other times it is difficult to distinguish levels, because of other pixel noise sources.

An algorithm was created to detect those pixels which jump in charge level by $\geq 430e^-$. Table 5 lists the number and percentage of pixels that exhibit these characteristics in a single data set. Typically, the same pixels exhibit popcorn noise over multiple data sets. However, the percentages may be a lower limit, since not all pixels with popcorn noise transition enough or with a large enough magnitude to be found by the routine every time. We have not examined the statistics for pixels which exhibit popcorn noise with level shifts of less than 430e^-.

This same behavior can be seen on "good" pixels, saturated pixels, reference pixels, and pixels with cosmic ray hits in forward bias (see Figure 9). Together with the large magnitude of the transitions, this leads to the

conclusion that the source of the noise lies within the multiplexer. Rockwell Scientific Company is investigating the multiplexer to determine the cause of the popcorn noise.

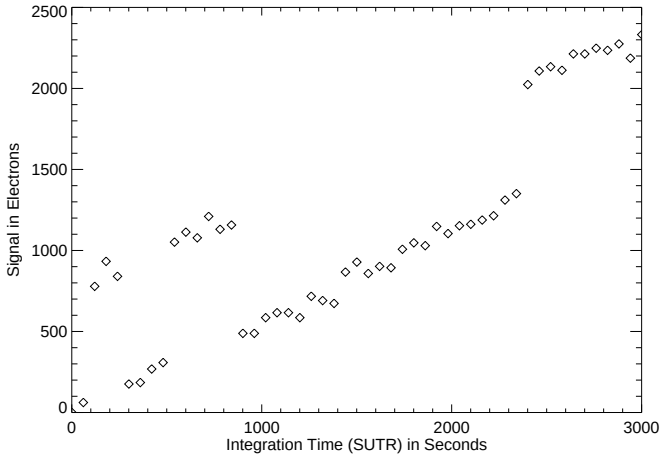

Figure 7. This figure shows dark charge vs. time in SUTR mode for a pixel on detector H1RG-16-002. This pixel exhibits *slow* transition popcorn noise. There are 60 seconds between points.

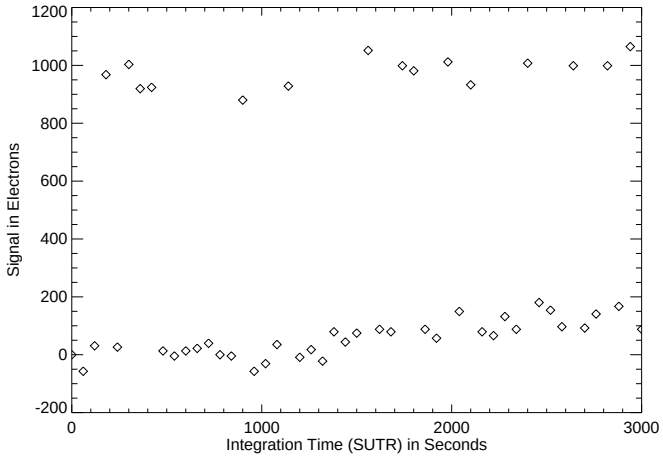

Figure 8. This figure shows dark charge vs. time in SUTR mode for a pixel on detector H1RG-16-002. This pixel exhibits *fast* transition popcorn noise. There are 60 seconds between points.

Table 5. This table shows the number and percentage of pixels for all three arrays that exhibit popcorn noise exceeding $430e^-$ in a single data set.

Pixels With Popcorn Noise in a Single Data Set

Detector	Number of Pixels	Percentage of Pixels
H1RG-16-001	1157	0.44%
H1RG-16-002	703	0.27%
H1RG-16-003	981	0.37%

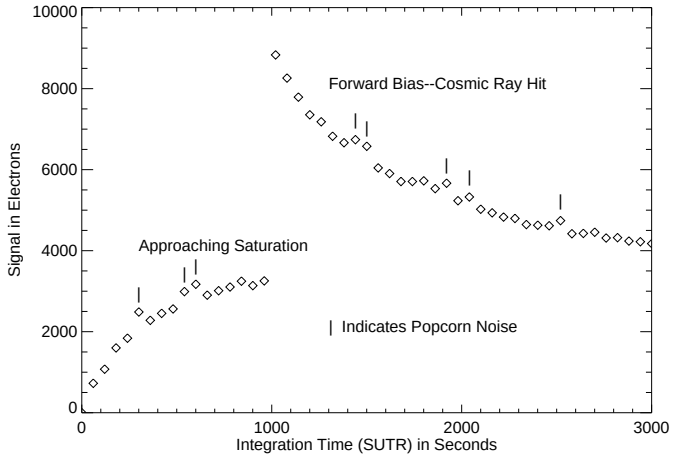

Figure 9. This figure shows dark charge vs. time in SUTR mode for a single pixel on detector H1RG-16-001. This pixel exhibits popcorn noise while approaching saturation and in forward bias after a cosmic ray hit. There are 60 seconds between points.

8. CONCLUSIONS

In this paper we report extensive characterization of three Rockwell Scientific Company LWIR HgCdTe detector arrays. The majority of the pixels exhibit exceedingly low dark currents, well below our goal of $30e^-/s$ while maintaining adequate well depth at lower applied biases. These same pixels also exhibit varying degrees of non-linearity. The average quantum efficiency per pixel of these detectors varies from 30% to 55%, which can be increased with the addition of anti-reflection coatings and microlenses.

With the proprietary technological advancements demonstrated in these detector arrays, future space astronomy missions employing passively cooled 10μm cutoff HgCdTe detector arrays are now possible. In future work we intend to obtain detector arrays with even longer cutoff wavelengths. In addition, for future detector array deliveries, anti-reflection coatings and microlenses will be applied to improve the average RQE. By advancing in these two areas, we will expand upon the already remarkable performance of these arrays.

ACKNOWLEDGMENTS

We are grateful for support for this program. Specifically we acknowledge NASA grant NAG5-6267 as well as NASA Ames grant NAG2-1333.

REFERENCES

1. A. D. Estrada, G. Domingo, J. D. Garnett, A. W. Hoffman, N. A. Lum, P. J. Love, S. L. Solomon, J. E. Venzon, G. R. Chapman, K. P. Sparkman, C. R. McCreight, M. E. McKelvey, R. E. McMurray, J. A. Estrada, S. Zins, R. McHugh, and R. Johnson, "Si:As IBC IR focal plane arrays for ground-based and space-based astronomy," in *Proc. SPIE, Infrared Astronomical Instrumentation*, A. M. Fowler, ed., **3354**, pp. 99–108, Aug. 1998.
2. C. M. Bacon, J. L. Pipher, W. J. Forrest, C. W. McMurtry, J. D. Garnett, D. Lee, and D. D. Edwall, "Characterization of Rockwell Scientific LWIR HgCdTe Detector Arrays," in *Proc. SPIE, Focal Plane Arrays for Space Telescopes.*, T. J. Grycewicz and C. R. McCreight, eds., **5167**, pp. 313–319, 2004.
3. C. M. Bacon, J. L. Pipher, W. J. Forrest, C. W. McMurtry, and J. D. Garnett, "Diode Characterization of Rockwell LWIR HgCdTe Detector Arrays," in *Proc. SPIE, IR Space Telescopes and Instruments.*, J. C. Mather, ed., **4850**, pp. 927–934, 2003.
4. R. B. Bailey, J. M. Arias, W. V. McLevige, J. G. Pasko, A. C. Chen, C. Cabelli, L. J. Kozlowski, K. Vural, J. Wu, W. J. Forrest, and J. L. Pipher, "Prospects for large-format IR astronomy FPAs using MBE-grown HgCdTe detectors with cutoff wavelength $> 4\mu$m," in *Proc. SPIE, Infrared Astronomical Instrumentation*, A. M. Fowler, ed., **3354**, pp. 77–86, Aug. 1998.
5. J. Wu, *Development of Infrared Detectors for Space Astronomy, PhD Thesis*, University of Rochester, Rochester, NY, 1997.
6. M. Loose, M. C. Farris, J. D. Garnett, D. N. B. Hall, and L. J. Kozlowski, "HAWAII-2RG: a 2k x 2k CMOS multiplexer for low and high background astronomy applications," in *Proc. SPIE, IR Space Telescopes and Instruments.*, J. C. Mather, ed., **4850**, pp. 867–879, 2003.
7. A. M. Fowler and I. Gatley, "Noise reduction strategy for hybrid IR focal-plane arrays," in *Proc. SPIE, Infrared Sensors: Detectors, Electronics, and Signal Processing*, T. S. Jayadev, ed., **1541**, pp. 127–133, Nov. 1991.
8. L. Mortara and A. Fowler, "Evaluations of CCD: Performance for Astronomical Use," *Proc. SPIE, Solid State Imagers for Astronomy* **290**, pp. 28–30, 1981.
9. J. L. Hora, G. G. Fazio, S. P. Willner, M. L. Ashby, J. Huang, S. T. Megeath, J. R. Stauffer, E. V. Tollestrup, Z. Wang, W. J. Glaccum, J. L. Pipher, W. J. Forrest, C. R. McCreight, M. E. McKelvey, W. F. Hoffman, P. Eisenhardt, J. A. Surace, W. T. Reach, S. H. Moseley, R. G. Arendt, K. P. Stewart, and F. D. Robinson, "Calibration and performance of the Infrared Array Camera (IRAC)," *Proc. SPIE, Infrared Spaceborne Remote Sensing VIII* **4131**, pp. 13–25, 2000.
10. G. H. Rieke, *Detection of Light from the Ultraviolet to the Submillimeter*, Cambridge University Press, Great Britain, 1994.
11. B. Pain and B. Hancock, "Accurate Estimation of Conversion Gain and Quantum Efficiency in CMOS Imagers," *Proc. SPIE, Sensors and Camera Systems for Scientific, Industrial, and Digital Photography Applications IV* **5017**, pp. 94–103, 2003.